*fluids*

MDPI

*Article*

# Lower-Dimensional Model of the Flow and Transport Processes in Thin Domains by Numerical Averaging Technique

**Maria Vasilyeva [1,*], Nana Adjoah Mbroh [1] and Mehrube Mehrubeoglu [2]**

[1] Department of Mathematics & Statistics, Texas A&M University-Corpus Christi, Corpus Christi, TX 78412, USA; nanaadjoah.mbroh@tamucc.edu
[2] Department of Engineering, Texas A&M University-Corpus Christi, Corpus Christi, TX 78412, USA; ruby.mehrubeoglu@tamucc.edu
* Correspondence: maria.vasilyeva@tamucc.edu

**Abstract:** In this work, we present a lower-dimensional model for flow and transport problems in thin domains with rough walls. The full-order model is given for a fully resolved geometry, wherein we consider Stokes flow and a time-dependent diffusion–convection equation with inlet and outlet boundary conditions and zero-flux boundary conditions for both the flow and transport problems on domain walls. Generally, discretizations of a full-order model by classical numerical schemes result in very large discrete problems, which are computationally expensive given that sufficiently fine grids are needed for the approximation. To construct a computationally efficient numerical method, we propose a model-order-reduction numerical technique to reduce the full-order model to a lower-dimensional model. The construction of the lower-dimensional model for the flow and the transport problem is based on the finite volume method and the concept of numerical averaging. Numerical results are presented for three test geometries with varying roughness of walls and thickness of the two-dimensional domain to show the accuracy and applicability of the proposed scheme. In our numerical simulations, we use solutions obtained from the finite element method on a fine grid that can resolve the complex geometry at the grid level as the reference solution to the problem.

**Keywords:** upscaling; coarse grid; flow and transport problem; thin domain

check for updates

**Citation:** Vasilyeva, M.; Mbroh, N.A.; Mehrubeoglu, M. Lower-Dimensional Model of the Flow and Transport Processes in Thin Domains by Numerical Averaging Technique. *Fluids* **2024**, *9*, 4. https://doi.org/10.3390/fluids9010004

Academic Editors: Giuliano De Stefano and D. Andrew S. Rees

Received: 2 November 2023
Revised: 11 December 2023
Accepted: 21 December 2023
Published: 25 December 2023

**Copyright:** © 2023 by the authors. Licensee MDPI, Basel, Switzerland. This article is an open access article distributed under the terms and conditions of the Creative Commons Attribution (CC BY) license (https://creativecommons.org/licenses/by/4.0/).

## 1. Introduction

Mathematical models for thin domains describe many real-world applications in science and engineering. In biological applications, simulation of blood and fluid flow in vessels can be described by fluid and transport problems in thin domains [1–3]. Flow simulation can study fluid flow in complex pipe structures, such as pipe-wise industrial installations, wells in the oil and gas industry, heat exchanges, etc. In reservoir simulations, thin domains are related to channels and fractures. Fractures have complex geometries with relatively small thicknesses compared to typical reservoir sizes [4–6]. Moreover, a comparatively small domain thickness provides significant complexity in grid construction, rendering classical numerical methods less practical.

To employ these classical numerical methods, such as the finite difference methods [7–9], finite volume methods [10,11], finite element methods [12–14], and mixed finite element methods [15,16], to simulate such problems, an extremely fine grid needs to be constructed to resolve the complex geometry structure at the grid level. This approach is usually computationally expensive because the discretization leads to a large discrete problem with several unknowns. In the process of addressing computational inefficiency, much research work has been done on the development of robust numerical methods. See, for example, the survey articles [17–19] and the references for the various types of numerical methods. Generally, two main procedures—namely, the use of parallel computing and the application of model-order-reduction techniques—are known. In parallel computing, multiple processors are used to concurrently execute numerous smaller computations

that are derived from larger, intricate problems, as employed in, for instance, the research articles [20–22], while multiscale model-order techniques lower the size of the model to reduce the computational domain [23–30]. The latter is employed in this paper.

Model reduction techniques usually depend on a coarse-grid approximation, which can be obtained by discretizing the problem onto a coarse grid and choosing a suitable coarse-grid formulation of the problem, which we implement here. One of the widely used ways is based on the numerical homogenization technique, whereby effective parameters are calculated in order to construct coarse-grid approximations [31,32]. Generally, these calculations are based on fine-grid results and are carefully done to mimic the fine-grid properties. Depending on the size of the area used in the calculations, upscaling techniques can be classified into local, extended local, and global approaches [25]. The local approach calculates effective parameters over specific coarse block areas. In the global approach, the global solution is used to calculate the effective parameters for the upscaled model to incorporate time–space variation and take into account nonlinearity. Apart from the target coarse block areas, neighboring regions are also used in the calculations for the extended local approach to obtain more accurate results. All these approaches have advantages and disadvantages [25,33–35]. In the local upscaling method, coarse-grid parameters are obtained independently of global solution information, leading to a computationally efficient approach. More accurate calculations should be based on information about the fine-scale solution and will lead to the global approach. For example, we can involve iterations between the global coarse-grid model and local fine-grid calculations to update the macroscale parameters [25]. This approach requires more computations than existing classic upscaling techniques, and some types of machine learning can be used to construct computationally efficient algorithms [36].

Several multiscale methods have been developed to obtain the coarse-grid formulation for the problems in heterogeneous domains, including multiscale finite element methods [26,30], mixed multiscale finite element methods [24], generalized multiscale finite element methods [27], multiscale mortar mixed finite element methods [28], multiscale finite volume methods [37,38], variational multiscale methods [39], and heterogeneous multiscale methods [40]. In [41], we proposed the Generalized Multiscale Finite Element Method (GMsFEM) to solve problems in perforated domains. We developed a multiscale procedure to identify multiscale basis functions in each coarse block using a snapshot space and local spectral problems. We apply our general concept to the Laplace, elasticity, and Stokes equations in perforated domains. The construction of a multiscale method for transport and flow processes in perforated domains is considered in [42], wherein we use the Mixed GMsFEM. In [43,44], we proposed the discontinuous Galerkin GMsFEM to solve the Laplace, elasticity, and Stokes equations.

In this work, we consider the numerical homogenization method, whereby averages of the effective properties of the materials are calculated and then used to approximate the solution on a coarse grid. This approach, although a model reduction technique, is different from the multiscale methods wherein multiscale basis functions are employed to extract information of the domain at the micro-level and then to bridge the information between the micro and macro scales [45,46]. We want to emphasize that this work seeks to contribute to the literature for robust numerical solutions for problems in the thin domain and is quite different from our previous works [45,46]. However, the idea of model reduction techniques was proposed to solve problems in thin domains.

In [45], the proposed model-order-reduction technique was based on the Discontinuous Galerkin Generalized Multiscale Finite Element Method (DG-GMsGEM). It was used to solve unsteady-state Stokes flow and transport problems in thin domains with reactive boundaries. A snapshot space for each interface between coarse-grid cells was constructed to capture possible flows. To reduce the snapshot space size, dimension reduction was performed using the local spectral problem with the corresponding eigenvectors of the smallest eigenvalues for the approximation on the coarse grid. For the transport problem, a multiscale basis function for each interface between coarse-grid cells was constructed,

and additional basis functions were also presented to capture non-homogeneous boundary conditions on walls. Subsequently, in our work [46], the Mixed Generalized Multiscale Finite Element Method based on multiscale basis functions for velocity fields was proposed to lower the dimension of an elliptic problem in a thin domain. To obtain the multiscale approximation, snapshot spaces were constructed for each interface between coarse-grid cells, and a local spectral problem was solved to identify the dominant modes in the snapshot space. The results obtained from the numerical experiment displayed good applicability of the proposed scheme, and we noted that the scheme allows the description of heterogeneities of the domain on the micro-level with high accuracy.

Motivated by our previous works [45,46], where multiscale finite element methods were developed to upscale an elliptic and unsteady state Stokes flow and transport problems in thin domains with reactive boundaries, we aim to investigate the steady-state Stokes flow and transport problems in thin domains. Additionally, motivated by [36,47,48], we present numerical upscaling based on the finite volume approximation on the coarse grid. Finite volume averaging is flexible, applicable under general conditions, and can produce accurate approximations to direct numerical simulation. Similarly to the multiscale finite volume method, numerical upscaling can consider the specific structure of the thin domain and construct an accurate macroscale characterization of the flow. In this paper, we aim to reduce the regular model with fully resolved geometry to a one-dimensional model. Thus, we propose a numerical averaging technique based on the finite volume method to construct the discrete problems on a coarse grid to lower the dimensions of both the flow and transport problems. Numerical simulations are conducted for three test geometries. In each instance, the results obtained from the finite element approximation on a fine grid are used as our reference solution.

The rest of the paper is organized as follows; Section 2 entails the problem formulation, which includes defining the domain, introducing the full-order model, and presenting the weak formulation of our finite element approximation. In Section 3, we present the lower-dimensional model and discuss the numerical averaging of both the flow and the transport problems. Section 4 presents the numerical simulations and discusses the results obtained, while the final section summarizes the paper.

## 2. Problem Formulation

Let $\Omega$ be a thin domain with multiscale features (rough boundary), for which the thickness is small compared to the domain length (See Figure 1). We let $\Gamma_{in}$ be an inflow boundary, $\Gamma_{out}$ be an outflow boundary, $\Gamma_w$ be the walled boundaries of the thin domain, and $\Gamma_w \cup \Gamma_{in} \cup \Gamma_{out} = \partial\Omega$.

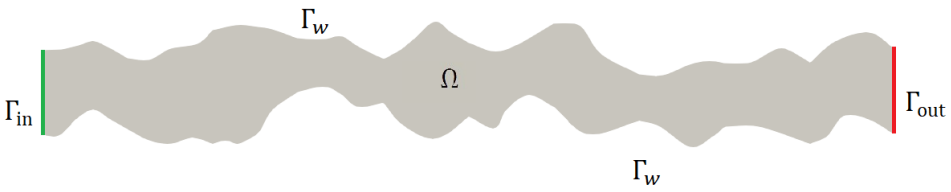



**Figure 1.** Illustration of a thin domain $\Omega$.

As indicated earlier, the solution obtained from a regular approach based on finite element discretization of the flow and the transport problem is the reference solution in our numerical simulations. Notice that for the finite element scheme to resolve the complex wall structure and the heterogeneity of the coefficients, a sufficiently large fine grid must be used for the discretization. Thus, we start with the regular model in full-geometry resolution and call it the full-order model (FOM).

### 2.1. Full-Order Model (FOM)

We consider the transport problem in the thin domain $\Omega$ given by the convection–diffusion equation:

$$\frac{\partial c}{\partial t} + \nabla \cdot (\mathbf{u}c) - \nabla \cdot (D\nabla c) = 0, \quad x \in \Omega, \quad t > 0. \tag{1}$$

where $x$ is the spatial variable, $c$ is the concentration, $D$ is the diffusion coefficient, and $\mathbf{u}$ is the fluid velocity.

For the fluid flow problem, we have the steady-state Stokes equations:

$$\begin{aligned} -\mu\Delta\mathbf{u} + \nabla p = 0, \quad x \in \Omega, \\ \nabla \cdot \mathbf{u} = 0, \quad x \in \Omega, \end{aligned} \tag{2}$$

where $\mu$ is the fluid viscosity, and $\mathbf{u}$ and $p$ are the velocity and pressure, respectively.

The system (1) and (2) is considered with the following initial conditions:

$$c = c_0, \quad x \in \Omega, \quad t = 0. \tag{3}$$

For the flow problem, we set the following boundary conditions:

$$p = p_{in} \text{ on } \Gamma_{in}, \quad p = p_{out} \text{ on } \Gamma_{out}, \quad \mathbf{u} = 0 \text{ on } \Gamma_w. \tag{4}$$

For the transport problem, we set

$$c = c_{in} \text{ on } \Gamma_{in}, \quad -D\nabla c \cdot n = 0 \text{ on } \Gamma_{out} \cup \Gamma_w, \tag{5}$$

where $n$ is the unit outward normal vector on $\partial\Omega$.

To solve a full-order model (1) and (2) with initial condition (3) and boundary conditions (4) and (5), we use a finite element method and start with a variational formulation.

### 2.2. Weak Formulation and Discrete FOM

Let $V = [H^1(\Omega)]^d$, $Q = H^1(\Omega)$, $P = L^2(\Omega)$ be an appropriate velocity, concentration, and pressure, respectively. The variational formulation of problems (1) and (2) with (3)–(5) is the following:

- Transport problem: find $c \in Q_c$ such that

$$m(c_t, r) + a(c, r) = 0, \quad \forall r \in Q_0 \tag{6}$$

with

$$\begin{aligned} m(c, r) &= (c, r)_\Omega, \\ a(c, r) &= (D\nabla c, \nabla r)_\Omega + (\nabla(\mathbf{u}c), r)_\Omega, \end{aligned}$$

and

$$Q_c = \{r \in Q : r = c_{in} \text{ on } \Gamma_{in}\}, \quad Q_0 = \{r \in Q : r = 0 \text{ on } \Gamma_{in}\},$$

- Flow problem: $(\mathbf{u}, p) \in V_0 \times P$ such that

$$\begin{aligned} s(\mathbf{u}, v) + b(v, p) = l(v), \quad \forall v \in V_0 \\ b(\mathbf{u}, q) = 0, \quad \forall q \in P \end{aligned} \tag{7}$$

with

$$\begin{aligned} s(\mathbf{u}, v) &= (\mu\nabla\mathbf{u}, \nabla v)_\Omega \\ b(v, q) &= -(q, \nabla \cdot v)_\Omega, \\ l(v) &= (p_{in} \cdot n, v)_{\Gamma_{in}} + (p_{out} \cdot n, v)_{\Gamma_{out}}, \end{aligned}$$

and

$$V_0 = \{v \in V : v = 0 \text{ on } \Gamma_w\}, \quad P = L^2(\Omega).$$

Let $\mathcal{T}^h$ be a fine-grid partition of the domain $\Omega$,

$$\mathcal{T}^h = \bigcup_{i=1}^{N_h} K_i,$$

where $N_h$ is the number of fine-grid cells. We use $\mathcal{E}^h$ to denote the set of facets in $\mathcal{T}^h$ with $\mathcal{E}^h = \mathcal{E}^h_o \cup \mathcal{E}^h_b$, where $\mathcal{E}^h_o$ is the set of interior facets, and $\mathcal{E}^h_b$ is the set of boundary facets, with $\mathcal{E}^h_b = \mathcal{E}^h_{b,in} \cup \mathcal{E}^h_{b,w} \cup \mathcal{E}^h_{b,out}$ (see Figure 2). We use the notations $K$ and $E$ to denote a generic cell and facet, respectively, in the fine grid $\mathcal{T}^h$. To define a discrete form of the problem, we can use different types of finite element approaches to approximate the flow and transport problems separately. For example, we can use Taylor–Hood elements for the fluid flow problem and the continuous Galerkin approximation for the transport problem.

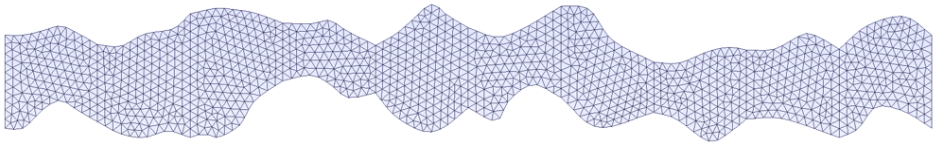


**Figure 2.** Fine grid for a full-order approximation (FOM).

Let $P_h$, $V_h$, and $Q_h$ be the fine-scale spaces for pressure, velocity, and concentration, respectively. After applying an implicit scheme for the time approximation in the transport problem, we have the following discrete problem, which can be solved to obtain the fine-scale result of the FOM problem:

- Transport problem: find $c_h \in Q_h$ such that

$$\frac{1}{\tau} m((c_h^{k+1} - c_h^k), r) + a(c_h^{k+1}, r) = 0, \quad \forall r \in Q_h, \tag{8}$$

with

$$m(c, r) = \sum_{K \in \mathcal{T}^h} \int_K c\, r\, dx, \quad a(c, r) = \sum_{K \in \mathcal{T}^h} \int_K (D \nabla c \cdot \nabla r + \nabla(\mathbf{u} c)\, r) dx.$$

- Flow problem: find $(\mathbf{u}_h, p_h) \in V_h \times P_h$ such that

$$\begin{aligned} s(\mathbf{u}_h, v) + b(p_h, v) &= l(v), \quad \forall v \in V_h, \\ b(\mathbf{u}_h, q) &= 0, \quad \forall q \in P_h, \end{aligned} \tag{9}$$

with

$$s(\mathbf{u}, v) = \sum_{K \in \mathcal{T}^h} \int_K \mu \nabla \mathbf{u} \colon \nabla v\, dx, \quad b(v, q) = -\sum_{K \in \mathcal{T}^h} \int_K q\, \nabla \cdot v\, dx,$$

$$l(v) = \sum_{E \in \mathcal{E}^h_{b,in}} \int_E p_{in} \cdot n\, v\, ds + \sum_{E \in \mathcal{E}^h_{b,out}} \int_E p_{out} \cdot n\, v\, ds.$$

Here, $k$ is the time iteration number, and $\tau$ is the fixed time-step size.

Note that in the considered model, the flow does not depend on concentration and can, therefore, be calculated at the beginning of the time iterations of the transport problem. More complex flow models can be considered with possible nonlinearity and time dependence.

In the next section, we present the proposed lower-order-reduction model and the numerical averaging scheme to solve the steady-state flow and transport problems.

## 3. Lower-Dimensional Model and Numerical Averaging

The full-order model considered above requires very fine grids that can resolve complex rough-walled geometries with variable thickness at the grid level. In this work, we propose an averaging technique to construct a lower-dimensional model (one-dimensional for $\Omega \in \mathcal{R}^2$). To construct a one-dimensional model, we calculate average fluxes numerically and construct a discrete problem using the coarse grid based on the finite volume method. We define local domains for each interface in the lower-dimensional model and calculate effective transmissibilities considering the fine-grid resolution of the rough boundaries and variable thickness.

Let $\mathcal{T}^H$ be a structured coarse mesh of the computational domain $\Omega$ (Figure 3).

$$\mathcal{T}^H = \bigcup_{i=1}^{N_H} K_i,$$

where $N_H$ is the number of the coarse-grid cells, $K_i$ is the coarse cell, and $i$ is the coarse-grid cell index.

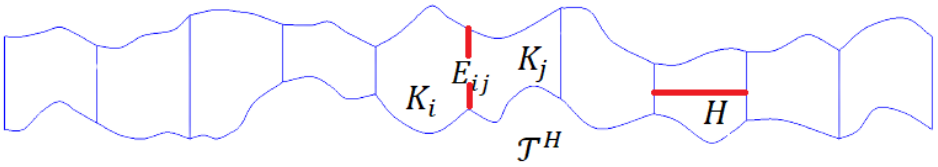



**Figure 3.** Coarse grid $\mathcal{T}^H$ with coarse cell $K_i$ and local domain $\omega_{ij} = K_i \cup K_j$, $E_{ij} = K_i \cap K_j$.

We let $E_{ij}$ be the coarse-grid facet and define the neighborhood (local domain) by

$$\omega_{ij} = \{K_i \cup K_j : K_i, K_j \in \mathcal{T}^H \text{ and } K_i \cap K_j = E_{ij}\},$$

where $\omega_{ij}$ is a union of two coarse cells when $E_{ij}$ lies in the interior of the domain $\Omega$ ($\Gamma_{in}$).

For the edges on the boundary $\Gamma_{out}$ or $\Gamma_{in}$, we have

$$\omega_{b,i} = \{K_i : K_i \in \mathcal{T}^H \text{ and } K_i \cap \Gamma_b = E_{b,i}\}$$

for $b = in, out$.

### 3.1. Flow Averaging

In each local domain $K_i$, we have a mass balance equation: $\nabla \cdot \mathbf{u} = 0$. After integrating over the local domain $K_i$ and taking into account no-flow boundary conditions on the wall boundaries, we obtain

$$\sum_{j=i-1,i+1} \bar{\mathbf{u}}_{ij} + \sum_{b=in,out} \bar{\mathbf{u}}_{b,i} = 0, \tag{10}$$

where $\bar{\mathbf{u}}_{ij}$ is the average flux on interface $E_{ij}$, and $\bar{\mathbf{u}}_{bi}$ is the average flux on the inlet and outlet boundaries

$$\bar{\mathbf{u}}_{ij} = \int_{E_{ij}} \mathbf{u} \cdot n \, ds, \quad \bar{\mathbf{u}}_{b,i} = \int_{E_{b,i}} \mathbf{u} \cdot n \, ds,$$

with $E_{in,i} = \Gamma_{in}$ and $E_{out,i} = \Gamma_{out}$.

Next, we use linear approximation to calculate the average fluxes:

$$\begin{aligned} \bar{\mathbf{u}}_{ij} &= \overline{T}_{ij}(\bar{p}_i - \bar{p}_j) \quad \text{with} \quad \overline{T}_{ij} = \frac{\int_{E_{ij}} \mathbf{u} \cdot n \, ds}{\bar{p}_i - \bar{p}_j}, \\ \bar{\mathbf{u}}_{b,i} &= \overline{T}_{b,i}(\bar{p}_i - \bar{p}_b) \quad \text{with} \quad \overline{T}_{b,i} = \frac{\int_{E_{b,i}} \mathbf{u} \cdot n \, ds}{\bar{p}_i - \bar{p}_b}, \end{aligned} \tag{11}$$

where $\overline{T}_{ij}$ and $\overline{T}_{b,i}$ are the coarse-grid transmissibilities, which can be calculated numerically for each interface; and $\bar{p}_i$ is the coarse cell average pressure:

$$\bar{p}_i = \frac{1}{|K_i|} \int_{K_i} p \, dx.$$

Therefore, we have the following discrete lower-dimensional flow problem:

$$\sum_{j=i-1,i+1} \overline{T}_{ij}(\bar{p}_i - \bar{p}_j) + \sum_{b=in,out} \overline{T}_{b,i}(\bar{p}_i - \bar{p}_b) = 0, \tag{12}$$

subject to the boundary conditions $p_{in} = 1$ and $p_{out} = 0$. We note that the discrete problem (12) is the finite volume approximation of the flow problem with a two-point flux approximation (TPFA). However, in the proposed method, we calculate upscaled transmissibilities using a fine-scale solution corresponding to the general flow model (2) in a rough-walled thin domain. Such approximations belong to nonlinear two-point flux approximation (NTPFA) methods. In [35], the NTPFA was proposed for upscaling full-tensor effects in Darcy's flow model.

The accuracy of upscaled transmissibilities depends on the fine solution in the local domain, which is the function of boundary conditions [25,34,35]. There exist two major approaches in transmissibility calculations: local and global. In the local approach, we utilize an offline calculation (pre-calculation) of transmissibilities by solving the local problem in each local domain $\omega$ ($\omega = \omega_{ij}$ or $\omega = \omega_{b,i}$):

$$\begin{aligned} -\mu\Delta\mathbf{u} + \nabla p = 0, \quad & x \in \omega, \\ \nabla \cdot \mathbf{u} = 0, \quad & x \in \omega, \end{aligned} \tag{13}$$

with given fixed boundary conditions: for example, $p = 1$ at the inlet, $p = 0$ at the outlet of $\omega$, and no flux at other boundaries. Since boundary conditions have major effects on numerical upscaling results, the local simulations are performed on the local domain up to fine-scale resolution of the rough boundaries. Then, the transmissibility is determined as an average flux from the interface from (11).

In the presented approach, calculation of the macroscale parameters is based on solving fine-scale local problems in each local domain associated with the coarse edge. Boundary conditions for the local problem play a significant role in the upscaling procedure [25]. One possible technique to increase accuracy is to enlarge a local domain (oversampled domain or extended domain). The oversampling technique can reduce the boundary layer effect, and the problem can still be solved purely locally [30,34,49]. Some other types of boundary conditions are used in practice: for example, some combination of the no-flow and fixed-pressure boundary conditions, periodic boundary conditions, and linear pressure. In general, such boundary conditions are based on the assumption of a local constant pressure difference over the local region. The global fine-scale solution can be used as a boundary condition in the local calculations to overcome this critical issue in the local–global approach [25,34]. However, incorporating global fine-scale solution information is computationally expensive because it requires performing local calculations for each interface at each time or nonlinear iteration. Some machine-learning-based techniques can be utilized for efficient calculations without losing accuracy as an implementation of a global approach [36]. In future works, we will revisit this approach for nonlinear flow models in heterogeneous domains with complex local geometries.

### 3.2. Transport Averaging

For the time-dependent transport problem, we apply the same averaging process and form the following discrete mass balance in each local domain $K_i$:

$$\frac{\bar{c}_i^{n+1} - \bar{c}_i^n}{\tau}|K_i| + \sum_{j=i-1,i+1} \overline{A}_{ij}(\bar{p}_i - \bar{p}_j) + \sum_{b=in,out} \overline{A}_{b,i}(\bar{p}_i - \bar{p}_b) + \sum_{j=i-1,i+1} \overline{D}_{ij}(\bar{c}_i^{n+1} - \bar{c}_j^{n+1}) + \overline{D}_{in,i}(\bar{c}_i^{n+1} - \bar{c}_{in}) = 0, \tag{14}$$

where

$$\bar{c}_i = \frac{1}{|K_i|}\int_{K_i} c\, dx.$$

To calculate coarse-scale parameters $\overline{A}_{ij}$ and $\overline{D}_{ij}$, the following approximation is used:

$$\overline{A}_{ij} = \bar{c}_{ij}\overline{T}_{ij}, \quad \overline{A}_{in,i} = \bar{c}_{in}\overline{T}_{in,i}, \quad \overline{A}_{out,i} = \bar{c}_i\overline{T}_{out,i}, \tag{15}$$

$$\overline{D}_{ij} = D|E_{ij}|/d_{ij}, \quad \overline{D}_{in,i} = D|E_{in,i}|/d_{in,i}. \tag{16}$$

where $|E_{ij}|$, $|E_{in,i}$ are the area of the interface between coarse-grid cells $K_i$ and $K_j$; $d_{ij}$, $d_{in,i}$ are the distance between coarse cell centers; $\overline{T}_{ij}$, $\overline{T}_{b,i}$ $(b = in, out)$ are the upscaled transmissibility from the flow problem (11); and $\bar{c}_{ij}$ is the upwind approximation. The fine-grid problem (1) is considered with initial condition (3) and boundary conditions (5), and the discrete problem (14) is considered with initial condition $c_i^0 = c_0$ with $c_0 = 0$. As boundary conditions, we set $c_0^n = c_{in}$ for the inlet boundary and zero flux on the outlet boundary with $c_{in} = 1$.

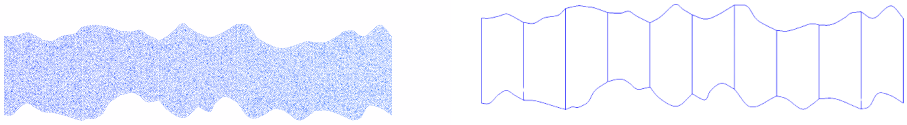
The considered approach is based on the upscaled linear transmissibility from the flow problem. The global coupled flow and transport information can be incorporated to improve the proposed method's accuracy. However, the global approach requires knowledge of the fine-scale distribution of the concentration field, which is unknown [25,34]. To overcome this issue, machine-learning-based algorithms can be constructed to predict accurate macroscale characteristics using coarse-grid information [36]. We will analyze and investigate numerically the local and global approaches in future works, as this is beyond the scope of the current paper.

## 4. Numerical Results

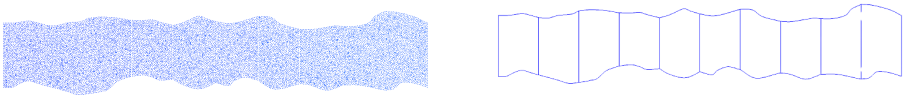
In this section, we present numerical results from simulations of lower-dimensional transport and flow models in a thin, rough-walled domain. The purpose of these simulations is to demonstrate the performance of the method presented in this paper. Numerical results were obtained from direct numerical simulations of the problems using three different geometries with full resolution. For each geometry, simulations were conducted using both the classical finite element method for the Stokes flow and transport problem on a fine-grid and the proposed upscaled one-dimensional scheme. The accuracy of the results obtained from the upscaled scheme was validated by calculating the errors between these results and those from the fine grid. Thus, throughout the simulations, the fine-grid solution serves as the reference solution for the upscaled solution, and the results in both scenarios are graphically displayed. Simulations were conducted for three different geometries, as displayed in Figure 4. Geometries 1 and 2 exhibit rougher boundaries than Geometry 3, and Geometry 2 is a thicker version of Geometry 1. For each geometry, we simulated results for three physical quantities: velocity, pressure, and concentration. For the flow problem, we computed upscaled results for velocity and pressure, while for the transport problem, computations were performed for the concentration at different time levels for all geometries.



(**a**) Geometry 1. Fine grid (left) and Coarse grid (right)



(**b**) Geometry 2. Fine grid (left) and Coarse grid (right)



(**c**) Geometry 3. Fine grid (left) and Coarse grid (right)

**Figure 4.** Geometries 1, 2, and 3.

Concentration and pressure errors between fine-grid solutions and upscaled solutions were computed using the relative errors in the $L^2$ norm:

$$e_c^H = \sqrt{\frac{\int_\Omega (\bar{c} - c)^2 dx}{\int_\Omega c^2 dx}} \times 100\%, \text{ and } e_p^H = \sqrt{\frac{\int_\Omega (\bar{p} - p)^2 dx}{\int_\Omega p^2 dx}} \times 100\%,$$

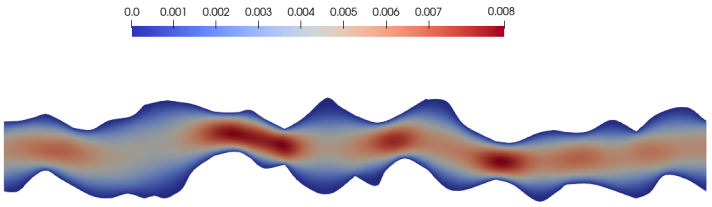
respectively, across all geometries. Here, $\bar{c}$, $\bar{p}$ are the upscaled solution and $c$, $p$ are the average fine-grid solution for concentration and pressure, respectively. Additionally, we calculate the velocity error

$$e_{\mathbf{u}}^H = \sqrt{\sum_{E_{ij}} \left( \int_{E_{ij}} \mathbf{u} \cdot n \, ds - \bar{\mathbf{u}}_{ij} \right)^2},$$

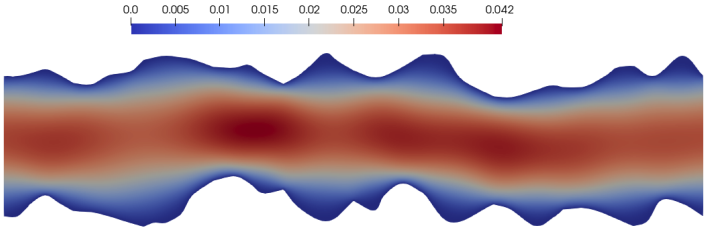
where $\bar{\mathbf{u}}_{ij}$ is the upscaled velocity on the given coarse-grid interface $E_{ij}$. Velocity and pressure errors are displayed in Table 1. The concentration errors are computed at different time levels for the three diffusion coefficients. The results are displayed in tables and figures to determine the effects of using different geometries. All numerical simulations were conducted using open-source libraries, including FEniCS [50], Gmsh [51], and Paraview [52].

The results for the Stokes flow problem for all geometries are presented in Figures 5 and 6 for both the fine-grid and upscaled solutions. Figure 5 displays solutions of the velocity whilst Figure 6 shows that of pressure. For Geometry 1, Figure 5a depicts the fine-grid solution for velocity, and both the fine-grid and upscaled solutions for pressure are displayed in Figure 5a. The fine-grid solution was achieved by constructing a two-dimensional grid consisting of 15,554 triangular cells and 8092 vertices, which can be observed on the left side of Figure 4a. In contrast, a one-dimensional coarse grid comprising 10 cells, shown on the right in Figure 4a, was employed to simulate the upscaled solution. For Geometry 2, the two-dimensional fine grid was composed of 32,594 triangular cells and 16,641 vertices, and a one-dimensional coarse grid with 10 cells was used to simulate the upscaled results. This can be observed in Figure 4b, while their solutions can also be seen in Figures 5b and 6b, respectively, for velocity and pressure. In addition, the

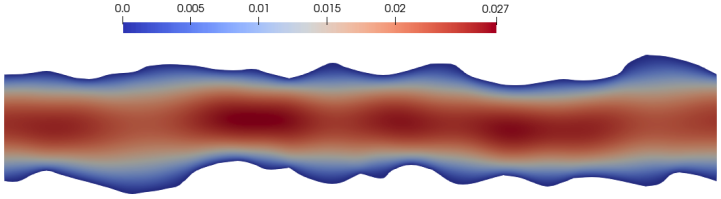
results for the last domain, Geometry 3, are given in Figure 5c for the fine-grid velocity and Figure 6c for the fine-grid and upscaled solution for pressure. Here, 25,607 triangular cells and 13,109 vertices were employed for the two-dimensional mesh construction, and similarly to Geometries 1 and 2, a one-dimensional coarse grid with 10 cells was employed for the upscaled solution. These are displayed in Figure 4c. This discretization approach enabled the fine grid to capture the complex geometry of our domain accurately. However, a significant amount of computational resources was required.




(**a**) Fine-grid velocity for Geometry 1

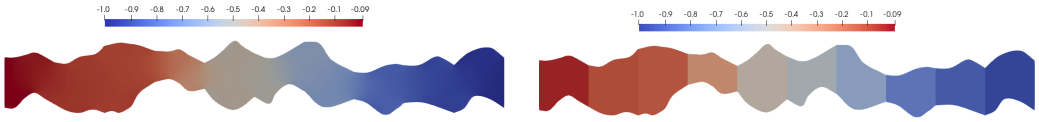



(**b**) Fine-grid velocity for Geometry 2

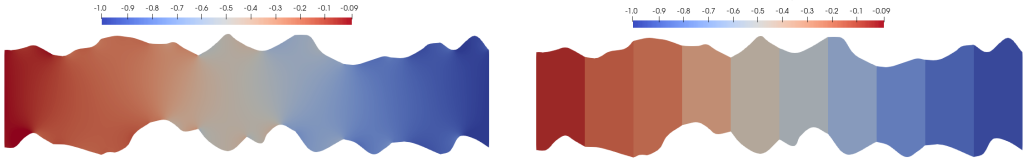



(**c**) Fine-grid velocity for Geometry 3

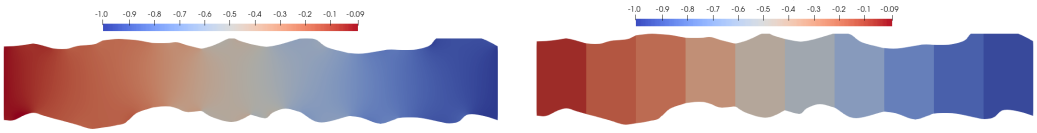
**Figure 5.** Velocities for Geometries 1, 2, and 3.




(**a**) Geometry 1. Fine-grid (left) and Upscaled pressure (right), $e_p^H = 0.35\%$




(**b**) Geometry 2. Fine-grid (left) and Upscaled pressure (right), $e_p^H = 0.06\%$




(**c**) Geometry 3. Fine-grid (left) and Upscaled pressure (right), $e_p^H = 0.03\%$

**Figure 6.** Fine-grid and Upscaled pressure for all geometries with 10 cells and $\mu = 0.1$.

**Table 1.** Pressure and velocity errors for all geometries for $\mu = 0.1$.

| | 5 Cells | | 10 Cells | |
|---|---|---|---|---|
| **Geometry** | $e_{\mathbf{u}}^H$ | $e_p^H$ | $e_{\mathbf{u}}^H$ | $e_p^H$ |
| 1 | 0.205 | 0.409 | 0.170 | 0.346 |
| 2 | 0.036 | 0.070 | 0.027 | 0.057 |
| 3 | 0.018 | 0.034 | 0.015 | 0.031 |

In our simulation of the flow problem, we set $\mu = 0.1$, assumed no-flow boundary conditions at the top and bottom boundaries, and used the values $\mathbf{u} = 0$, for the initial velocity and $p_{in} = 1$, $p_{out} = 0$ for the inflow boundary and outflow boundary conditions, respectively.

Upscaled velocity results exhibit high accuracy with minimal velocity error margins of 0.170%, 0.0274%, and 0.015% for Geometries 1, 2, and 3, respectively, with 10 cells. These results can also be confirmed through the corresponding entries in Table 1. These results clearly show that Geometry 1 produced the highest errors, followed by Geometry 3 and then Geometry 2. However, the differences are not significant. Results for the upscaled model for pressure are highly accurate, with 0.35%, 0.06%, and 0.03 % pressure errors for Geometries 1, 2 and 3, respectively, which can also be observed from Table 1. From Table 1, we can see that simulations with Geometry 3 produced the smallest errors, followed by Geometry 2 and then Geometry 1. These results indicate that thinner geometries yield more significant errors, while larger geometries produce minor errors. However, despite Geometry 2 being more accurate than Geometry 3, the pressure error was greater than that of Geometry 3. This could be explained by the fact that the boundaries of Geometry 2 showed more roughness than that of Geometry 3, which could contribute to the error. Although Geometry 1 produced the highest error, its value is still small. Thus, the proposed upscaling technique demonstrates a strong match to the fine-grid model with high accuracy and significantly reduces the size of the discrete system.

To assess the effect of mesh resolution on the upscaled results, we consider simulations for a one-dimensional upscaled model with 5 cells in addition to those performed with 10 cells. Velocity errors of 0.205%, 0.036% and 0.018% were obtained, and pressure errors of 0.41%, 0.07%, and 0.03% were observed for Geometries 1, 2, and 3, respectively. These results are also presented in Table 1, where velocity and pressure errors for $\mu = 0.1$ are tabulated. Errors obtained using 5 cells are higher than those found using 10 cells, indicating that a lower mesh resolution yields more errors than a higher mesh resolution. Furthermore, the influence of two different values of $\mu = 0.2$ and $\mu = 0.05$ was investigated to understand the impact on the results. Interestingly, our experiments revealed that values of both $\mu = 0.2$ and $\mu = 0.05$ produced the same errors as $\mu = 0.1$, indicating that $\mu$ does not affect the velocity and pressure errors.

The results for the transport equation for all geometries are presented in Figures 7–15 for the three diffusion coefficients: $D = 10^{-4}$, $D = 10^{-5}$ and $D = 10^{-6}$. Figures 7, 10, and 13 display the outcomes obtained with a diffusion coefficient of $D = 10^{-6}$, while Figures 9, 12, and 15 illustrate the results obtained with $D = 10^{-4}$. Results obtained with $D = 10^{-5}$ are presented in Figures 8, 11, and 14. These figures display both the reference fine-grid solution and the upscaled model solution. From the results, we can observe accurate solutions for the upscaling methodology.

In our simulation, the inflow and outflow concentration was set to $c_{in} = 1.0$, and 0.0 was set as the initial concentration. Throughout the simulations, it was evident that among the three geometries, the thinnest domain—Geometry 1—required an extended time for the concentration to diffuse completely within the entire domain, while the other two domains—Geometries 2 and 3—required a shorter time. A maximum time of 90 with 60 iterations was used in the simulation of Geometry 1, and the concentration at the time steps $t_{10}$, $t_{30}$, $t_{60}$ for both the fine-grid and the upscaled solution are displayed in the figures. For the thicker domains—Geometries 2 and 3—a maximum time of 20

with 60 iterations was used in the simulations, and the results of the concentrations at the time steps $t_{10}$, $t_{30}$, $t_{60}$ are displayed. These choices of maximum time and time steps were influenced by the fact that concentrations in the thinner domains required a longer time to diffuse through the entire domain, while the opposite was required in the thicker domains. Relative errors for concentrations between the fine-grid solutions and the upscaled solutions for all geometries were also calculated, and the results are displayed in Figure 16 and Tables 2–4 for some time levels. The error decreases with increased time. Also, it can be observed that Geometry 1 produced the smallest errors, followed closely by Geometry 3 and finally Geometry 2, although the differences were not significant.

**Table 2.** Geometry 1: Concentration errors at different time levels for all diffusion coefficients with $\mu = 0.1$.

| **Time** | $e_c^H$**, 5 Cells** | | | $e_c^H$**, 10 Cells** | | |
|---|---|---|---|---|---|---|
| $t_5 = 7.5$ | 46.132 | 18.269 | 8.667 | 33.815 | 21.945 | 17.578 |
| $t_{10} = 15$ | 38.628 | 19.304 | 16.034 | 20.948 | 17.505 | 12.308 |
| $t_{30} = 45$ | 28.550 | 32.364 | 28.821 | 9.508 | 8.808 | 4.049 |
| $t_{40} = 60$ | 23.759 | 27.103 | 21.474 | 8.010 | 7.252 | 7.256 |
| $t_{60} = 90$ | 19.657 | 21.544 | 14.187 | 7.790 | 7.931 | 11.826 |
| | $D = 10^{-4}$ | $D = 10^{-5}$ | $D = 10^{-6}$ | $D = 10^{-4}$ | $D = 10^{-5}$ | $D = 10^{-6}$ |



(**a**) Fine-grid (right) and Upscaled concentration (right) at $t_{10} = 15$, $e_c^H = 12.3\%$



(**b**) Fine-grid (left) and Upscaled concentration (right) at $t_{30} = 45$, $e_c^H = 4.0\%$



(**c**) Fine-grid (left) and Upscaled concentration (right) at $t_{60} = 90$, $e_c^H = 11.8\%$

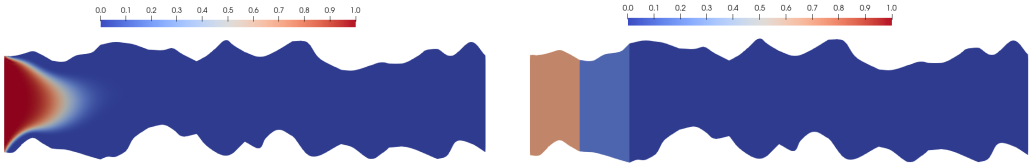
**Figure 7.** Geometry 1: Solutions in rough-walled thin domain with $D = 10^{-6}$, $\mu = 0.1$, and 10 cells.



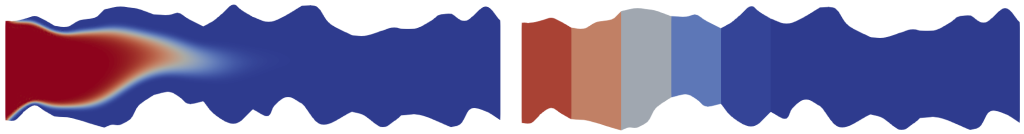
**Figure 8.** Geometry 1: Solutions in rough-walled thin domain with $D = 10^{-5}$, $\mu = 0.1$, and 10 cells. Fine-grid (**left**) and Upscaled concentration (**right**) at $t_{60} = 90$, $e_c^H = 7.9\%$.



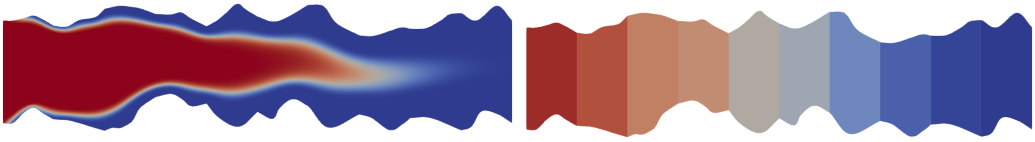
**Figure 9.** Geometry 1: Solutions in rough-walled thin domain with $D = 10^{-4}$, $\mu = 0.1$, and 10 cells. Fine-grid (**left**) and Upscaled concentration (**right**) at $t_{60} = 90$, $e_c^H = 7.8\%$.



(**a**) Fine-grid (left) and Upscaled concentration (right) at $t_{10} = 3.3$, $e_c^H = 17.4\%$



(**b**) Fine-grid (left) and Upscaled concentration (right) at $t_{30} = 10$, $e_c^H = 7.5\%$



(**c**) Fine-grid (left) and Upscaled concentration (right) at $t_{60} = 20$, $e_c^H = 12.2\%$

**Figure 10.** Geometry 2: Solutions in rough-walled thin domain with $D = 10^{-6}$.

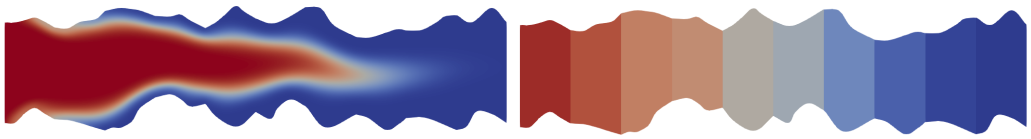


**Figure 11.** Geometry 2: Solutions in rough-walled thin domain with $D = 10^{-5}$. Fine-grid (**left**) and Upscaled concentration (**right**) at $t_{60} = 20$, $e_c^H = 12.2\%$.

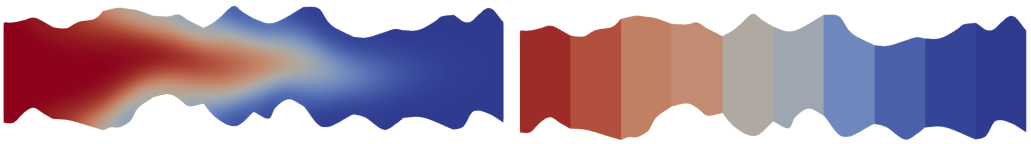
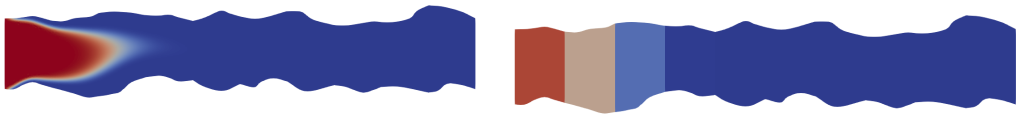


**Figure 12.** Geometry 2: Solutions in rough-walled thin domain with $D = 10^{-4}$. Fine-grid (**left**) and Upscaled concentration (**right**) at $t_{60} = 20$, $e_c^H = 12.1\%$.



(**a**) Fine-grid (left) and Upscaled concentration (right) at $t_{10} = 3.3$, $e_c^H = 24.5\%$



(**b**) Fine-grid (left) and Upscaled concentration (right) at $t_{30} = 10$, $e_c^H = 14.1\%$



(**c**) Fine-grid (left) and Upscaled concentration (right) at $t_{60} = 20$, $e_c^H = 8.4\%$

**Figure 13.** Geometry 3: Solutions in rough-walled thin domain with $D = 10^{-6}$.



**Figure 14.** Geometry 3: Solutions in rough-walled thin domain with $D = 10^{-5}$. Fine-grid (**left**) and Upscaled concentration (**right**) at $t_{60} = 20$, $e_c^H = 8.4\%$.



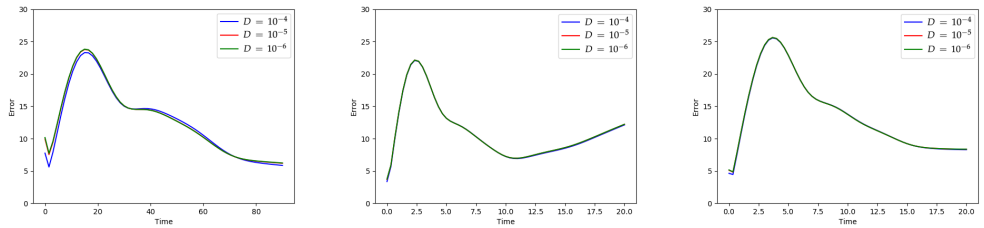
**Figure 15.** Geometry 3: Solutions in rough-walled thin domain with $D = 10^{-4}$. Fine-grid (**left**) and Upscaled concentration (**right**) at $t_{60} = 20$, $e_c^H = 8.3\%$.

**Table 3.** Geometry 2: Concentration errors at different time levels for all diffusion coefficients with $\mu = 0.1$.

| **Time** | $e_c^H$**, 10 Cells** | | |
|---|---|---|---|
| $t_5 = 1.6$ | 17.290 | 17.398 | 17.578 |
| $t_{10} = 3.3$ | 21.041 | 21.073 | 17.409 |
| $t_{30} = 10$ | 7.505 | 7.521 | 7.522 |
| $t_{40} = 13.3$ | 8.01 | 7.252 | 7.757 |
| $t_{50} = 16.6$ | 9.547 | 9.646 | 9.656 |
| $t_{60} = 20$ | 12.113 | 12.209 | 12.218 |
| | $D = 10^{-4}$ | $D = 10^{-5}$ | $D = 10^{-6}$ |

**Table 4.** Geometry 3: Concentration errors at different time levels for all diffusion coefficients with $\mu = 0.1$.

| **Time** | $e_c^H$**, 10 Cells** | | |
|---|---|---|---|
| $t_5 = 1.6$ | 13.672 | 13.880 | 13.901 |
| $t_{10} = 3.3$ | 24.384 | 24.477 | 24.486 |
| $t_{30} = 10$ | 14.177 | 14.139 | 14.136 |
| $t_{40} = 13.3$ | 10.836 | 10.807 | 10.804 |
| $t_{50} = 16.6$ | 8.544 | 8.577 | 8.581 |
| $t_{60} = 20$ | 8.282 | 8.357 | 8.365 |
| | $D = 10^{-4}$ | $D = 10^{-5}$ | $D = 10^{-6}$ |




(**a**) Geometry 1 (**b**) Geometry 2 (**c**) Geometry 3

**Figure 16.** Concentration errors for all diffusion coefficients in Geometries 1, 2, and 3 with 10 cells.

In addition, simulation results obtained with Geometry 1 are presented in Figures 7–9 for the diffusion coefficients $D = 10^{-6}$, $D = 10^{-5}$ and $D = 10^{-4}$, respectively. From the figures, it can be observed that the upscaled solution results gave a satisfactory approximation of the fine-grid solution. The computed errors associated with all three diffusion coefficients are given in Figure 16a and Table 2. From the figure, it is clear that the errors are converging to a smaller value, and also, the choice of diffusion coefficient does not have any significant effect on the results.

To determine the effect of the mesh resolution on the concentration for the upscaled results, additional simulations were conducted with Geometry 1 using a lower mesh resolution of 5 cells. The values of all other parameters remained the same. Table 2 displays the concentration errors for Geometry 1 and shows that simulations with 5 cells produced higher errors than those obtained with 10 cells, highlighting a significant influence of mesh resolution on the proposed upscaled scheme in this geometry.

As previously mentioned, Geometry 2 has a greater width compared to Geometry 1 and 3, and this characteristic leads to an accelerated diffusion rate of the concentration throughout the entire domain. The simulation results for this particular domain are displayed in Figures 10–12. A high level of accuracy in the method we have introduced can be observed from the result. The concentration errors between the fine-grid solutions and the upscaled solutions for the three diffusion values are presented in Figure 16b and Table 3. This graph shows that errors are increasing in this domain, and this could be justified by the fact that this domain has very rough boundaries and a shorter time was used in the simulation. Similar to the previous domain, the performance of the proposed upscaled method in this domain does not depend on the value of the diffusion coefficient.

In Geometry 3, we consider a domain with smoother walls, and the simulated results are displayed in Figures 13–15 for the three diffusion coefficients. Satisfactory performance of the proposed technique can be seen from the graphs, which can also be confirmed by Table 4 and Figure 16c. Table 4 and Figure 16c display the errors between the fine-grid solution and the upscaled solution for each diffusion coefficient. From Figure 16c, we can observe that the errors converge to a smaller value, and this observation can be confirmed by the results in Table 4. Similar to Geometry 2, the concentration required shorter time steps to diffuse into the entire domain, and the results do not depend on the value of the diffusion coefficients.

Furthermore, simulations were conducted with two additional viscosities, $\mu = 0.2$ and $\mu = 0.08$, to analyze the effect of viscosity on the upscaled concentration for Geometry 1. We consider diffusion values of $D = 10^{-6}, 10^{-5}$, and $10^{-4}$ and both the 5- and 10-cell resolutions. Results for both fine and upscaled concentration at the final times are shown in Figure 17a,c. Concentration results obtained with $\mu = 0.2$ are given in Figure 17 for the 5- and 10-cell resolutions, respectively. Whilst those for $\mu = 0.08$ are displayed in Figure 18a,c. We obtain faster flow with lower viscosity and observe that the concentration moves faster. In addition, concentration errors are displayed in Tables 5 and 6 for $\mu = 0.2$ and $\mu = 0.08$, respectively. We observe that errors obtained for $\mu = 0.08$ are lower than those of $\mu = 0.2$ with a very notable difference.



(**a**) Fine-scale (left) and upscaled concentration for 5 cells (middle) and 10 cells (right) for $D = 10^{-6}$.



(**b**) Fine-scale (left) and upscaled concentration for 5 cells (middle) and 10 cells (right) for $D = 10^{-5}$.



(**c**) Fine-scale (left) and upscaled concentration for 5 cells (middle) and 10 cells (right) for $D = 10^{-4}$.

**Figure 17.** Geometry 1: Solutions at final time in rough-walled thin domain with 5 and 10 cells for $\mu = 0.2$.



(**a**) Fine-scale (left) and upscaled concentration for 5 cells (middle) and 10 cells (right) for $D = 10^{-6}$.



(**b**) Fine-scale (left) and upscaled concentration for 5 cells (middle) and 10 cells (right) for $D = 10^{-5}$.



(**c**) Fine-scale (left) and upscaled concentration for 5 cells (middle) and 10 cells (right) for $D = 10^{-4}$.

**Figure 18.** Geometry 1: Solutions at final time in rough-walled thin domain with 5 and 10 cells for $\mu = 0.08$.

**Table 5.** Geometry 1: Concentration errors at different time levels with $\mu = 0.2$.

| **Time** | $e_c^H$**, 5 Cells** | | | $e_c^H$**, 10 Cells** | | |
|---|---|---|---|---|---|---|
| $t_5 = 7.5$ | 65.168 | 31.835 | 9.193 | 65.736 | 32.445 | 12.301 |
| $t_{10} = 15$ | 55.802 | 25.090 | 10.064 | 55.486 | 30.388 | 17.361 |
| $t_{30} = 45$ | 39.642 | 28.130 | 23.761 | 31.631 | 28.287 | 24.393 |
| $t_{40} = 60$ | 34.509 | 31.928 | 29.447 | 25.380 | 23.440 | 17.938 |
| $t_{60} = 90$ | 26.750 | 33.890 | 30.706 | 18.733 | 19.813 | 16.142 |
| | $D = 10^{-4}$ | $D = 10^{-5}$ | $D = 10^{-6}$ | $D = 10^{-4}$ | $D = 10^{-5}$ | $D = 10^{-6}$ |

**Table 6.** Geometry 1: Concentration errors at different time levels with $\mu = 0.08$.

| **Time** | $e_c^H$**, 5 Cells** | | | $e_c^H$**, 10 Cells** | | |
|---|---|---|---|---|---|---|
| $t_5 = 7.5$ | 38.178 | 15.867 | 9.918 | 39.113 | 42.317 | 16.578 |
| $t_{10} = 15$ | 34.450 | 21.723 | 19.139 | 29.427 | 31.844 | 21.889 |
| $t_{30} = 45$ | 24.941 | 27.749 | 22.398 | 13.488 | 13.921 | 10.612 |
| $t_{40} = 60$ | 21.387 | 22.618 | 17.039 | 11.548 | 11.817 | 6.251 |
| $t_{60} = 90$ | 18.919 | 18.162 | 10.829 | 9.852 | 9.955 | 7.276 |
| | $D = 10^{-4}$ | $D = 10^{-5}$ | $D = 10^{-6}$ | $D = 10^{-4}$ | $D = 10^{-5}$ | $D = 10^{-6}$ |

In our simulations, direct numerical simulations using finite element discretization on the fine grid—serving as our reference solution for the steady-state Stokes flow and transport problems—proved less computationally efficient than the upscaled simulations. For Geometry 1, the fine-grid simulations utilized 63,474 degrees of freedom for velocity, 8092 for pressure, and 8092 for concentration. In contrast, the upscaled results were achieved with a one-dimensional domain containing 10 or 5 cells for both the pressure and concentration equations.

For Geometry 2, the fine-grid solutions involved 131,750 degrees of freedom for velocity, 16,641 for pressure, and 16,641 for concentration. For Geometry 3, 103,648 degrees of freedom were employed for velocity and 13,109 for pressure and concentration. These large numbers of degrees of freedom highlight the substantial size of discrete systems and introduce numerous unknowns, especially compared to the upscaled one-dimensional formulation with 10 or 5 cells. Consequently, the computational cost is expected to be significantly higher than that of the one-dimensional upscaled approximation. This is evident in the computational time summaries provided in Table 7, where notable differences in computational times are recorded between fine and upscaled simulations. The upscaled results exhibit significantly lower computational times compared to the fine-grid solutions, which show higher computational times.

**Table 7.** Computational times in seconds for fine-grid and upscaled coarse-grid simulations, $\mu = 0.1$.

| Geometries | Flow Problem | | | Transport Problem | | |
|---|---|---|---|---|---|---|
| | Fine Grid | Upscaled | | Fine Grid | Upscaled | |
| | | 5 Cells | 10 Cells | | 5 Cells | 10 Cells |
| 1 | 21.171 | 0.032 | 0.055 | 12.472 | 0.136 | 0.143 |
| 2 | 99.444 | 0.036 | 0.031 | 31.673 | 0.126 | 0.137 |
| 3 | 57.961 | 0.040 | 0.070 | 25.892 | 0.138 | 0.155 |

## 5. Conclusions

In this paper, a model-order-reduction technique was presented to solve the flow and transport problems in thin domains. The method employs a numerical averaging approach based on the finite volume method. This technique effectively reduces the dimensionality of the full two-dimensional model to a one-dimensional representation. In constructing the one-dimensional model, numerical computations were used to determine the average flux, and finite volume discretization was performed on a coarse grid. This approach for solving problems in complex thin domains gives an accurate approximation of the steady-state Stokes flow and transport problems; this can be confirmed by the minor errors obtained from the simulations. For the fine-grid approximation, we applied the continuous Galerkin method and used the solution as a reference solution. To validate the practical performance of this method, numerical simulations were conducted on three different test geometries. The proposed model-order-reduction technique provides satisfactory results with only minor errors and gives a substantial reduction in the size of the system, which automatically reduces the computational time. The presented model can be used to reduce computation time while providing a simplified and usable coarse model for thin boundary problem applications.

As a future direction for this research, we are actively investigating the application of the proposed scheme to address fractional transport problems [53–55] and to extend its utility to a broader range of fractional problems [56–58]. Moreover, we are interested in considering reactive transport processes in thin domains with application to the complex structures of rough fractures [53,59].

**Author Contributions:** Conceptualization, M.V. and M.M.; Methodology, M.V.; Software, M.V.; Validation, N.A.M.; Investigation, N.A.M.; Writing—original draft, M.V., N.A.M. and M.M.; All authors have read and agreed to the published version of the manuscript.

**Funding:** This research received no external funding.

**Data Availability Statement:** Data are contained within the article.

**Conflicts of Interest:** The authors declare no conflicts of interest.

## References

1. Quarteroni, A.; Formaggia, L. Mathematical modelling and numerical simulation of the cardiovascular system. *Handb. Numer. Anal.* **2004**, *12*, 3–127.
2. Nachit, A.; Panasenko, G.P.; Zine, A. Asymptotic partial domain decomposition in thin tube structures: numerical experiments. *Int. J. Multiscale Comput. Eng.* **2013**, *11*, 407–441. [CrossRef]
3. Oshima, M.; Torii, R.; Kobayashi, T.; Taniguchi, N.; Takagi, K. Finite element simulation of blood flow in the cerebral artery. *Comput. Methods Appl. Mech. Eng.* **2001**, *191*, 661–671. [CrossRef]
4. Martin, V.; Jaffré, J.; Roberts, J.E. Modeling fractures and barriers as interfaces for flow in porous media. *SIAM J. Sci. Comput.* **2005**, *26*, 1667–1691. [CrossRef]
5. Formaggia, L.; Fumagalli, A.; Scotti, A.; Ruffo, P. A reduced model for Darcy's problem in networks of fractures. *ESAIM Math. Model. Numer. Anal.* **2014**, *48*, 1089–1116. [CrossRef]
6. D'angelo, C.; Quarteroni, A. On the coupling of 1d and 3d diffusion-reaction equations: application to tissue perfusion problems. *Math. Model. Methods Appl. Sci.* **2008**, *18*, 1481–1504. [CrossRef]
7. Levy, H.; Lessman, F. *Finite Difference Equations*; Courier Corporation: Chelmsford, MA, USA, 1992.
8. Dimov, I.; Faragó, I.; Vulkov, L. *Finite Difference Methods, Theory and Applications*; Springer: Berlin/Heidelberg, Germany, 2015.

9. Thomas, J.W. *Numerical Partial Differential Equations: Finite Difference Methods*; Springer Science & Business Media: Berlin/Heidelberg, Germany, 2013; Volume 22,
10. Moukalled, F.; Mangani, L.; Darwish, M.; Moukalled, F.; Mangani, L.; Darwish, M. *The Finite Volume Method*; Springer: Berlin/Heidelberg, Germany, 2016.
11. Eymard, R.; Gallouët, T.; Herbin, R. Finite volume methods. *Handb. Numer. Anal.* **2000**, *7*, 713–1018.
12. Dhatt, G.; Lefrançois, E.; Touzot, G. *Finite Element Method*; John Wiley & Sons: Hoboken, NJ, USA, 2012.
13. Zienkiewicz, O.C.; Taylor, R.L. *The Finite Element Method: Solid Mechanics*; Butterworth-Heinemann: Oxford, UK, 2000; Volume 2.
14. Zienkiewicz, O.C.; Taylor, R.L.; Zhu, J.Z. *The Finite Element Method: Its Basis and Fundamentals*; Elsevier: Amsterdam, The Netherlands, 2005.
15. Boffi, D.; Brezzi, F.; Fortin, M. *Mixed Finite Element Methods and Applications*; Springer: Berlin/Heidelberg, Germany, 2013; Volume 44.
16. Raviart, P.A.; Thomas, J.M. A mixed finite element method for 2-nd order elliptic problems. In *Mathematical Aspects of Finite Element Methods, Proceedings of the Conference, Rome, Italy, 10–12 December 1975*; Springer: Berlin/Heidelberg, Germany, 2006; pp. 292–315.
17. Lasseux, D.; Valdés-Parada, F.J.; Wood, B.D. Recent developments in upscaling and characterization of flow and transport in porous media. *Adv. Water Resour.* **2021**, *150*, 1–5. [CrossRef]
18. Vereecken, H.; Kasteel, R.; Vanderborght, J.; Harter, T. Upscaling hydraulic properties and soil water flow processes in heterogeneous soils: A review. *Vadose Zone J.* **2007**, *6*, 1–28. [CrossRef]
19. Zhang, X.; Ma, F.; Yin, S.; Wallace, C.D.; Soltanian, M.R.; Dai, Z.; Ritzi, R.W.; Ma, Z.; Zhan, C.; Lü, X. Application of upscaling methods for fluid flow and mass transport in multi-scale heterogeneous media: A critical review. *Appl. Energy* **2021**, *303*, 117603. [CrossRef]
20. Cliffe, K.; Graham, I.G.; Scheichl, R.; Stals, L. Parallel computation of flow in heterogeneous media modelled by mixed finite elements. *J. Comput. Phys.* **2000**, *164*, 258–282. [CrossRef]
21. Douglas, J.; Leme, P.P.; Roberts, J.; Wang, J. A parallel iterative procedure applicable to the approximate solution of second order partial differential equations by mixed finite element methods. *Numer. Math.* **1993**, *65*, 95–108. [CrossRef]
22. Hussain, M.; Abid, M.; Ahmad, M.; Hussain, S. A parallel 2D stabilized finite element method for Darcy flow on distributed systems. *World Appl. Sci. J.* **2013**, *27*, 1119–1125.
23. Aarnes, J.E. On the use of a mixed multiscale finite element method for greaterflexibility and increased speed or improved accuracy in reservoir simulation. *Multiscale Model. Simul.* **2004**, *2*, 421–439. [CrossRef]
24. Chen, Z.; Hou, T. A mixed multiscale finite element method for elliptic problems with oscillating coefficients. *Math. Comput.* **2003**, *72*, 541–576. [CrossRef]
25. Chen, Y.; Durlofsky, L.J.; Gerritsen, M.; Wen, X.H. A coupled local–global upscaling approach for simulating flow in highly heterogeneous formations. *Adv. Water Resour.* **2003**, *26*, 1041–1060. [CrossRef]
26. Efendiev, Y.; Hou, T.Y. *Multiscale Finite Element Methods: Theory and Applications*; Springer Science & Business Media: Berlin/Heidelberg, Germany, 2009; Volume 4.
27. Efendiev, Y.; Galvis, J.; Hou, T.Y. Generalized multiscale finite element methods (GMsFEM). *J. Comput. Phys.* **2013**, *251*, 116–135. [CrossRef]
28. Arbogast, T.; Pencheva, G.; Wheeler, M.F.; Yotov, I. A multiscale mortar mixed finite element method. *Multiscale Model. Simul.* **2007**, *6*, 319–346. [CrossRef]
29. Hernández, J.; Oliver, J.; Huespe, A.E.; Caicedo, M.; Cante, J. High-performance model reduction techniques in computational multiscale homogenization. *Comput. Methods Appl. Mech. Eng.* **2014**, *276*, 149–189. [CrossRef]
30. Hou, T.Y.; Wu, X.H. A multiscale finite element method for elliptic problems in composite materials and porous media. *J. Comput. Phys.* **1997**, *134*, 169–189. [CrossRef]
31. Bakhvalov, N.; Panasenko, G. *Homogenization in Periodic Media, Mathematical Problems of the Mechanics of Composite Materials*; NAUKA: Moscow, Russian, 1984.
32. Sánchez-Palencia, E. *Non-Homogeneous Media and Vibration Theory*; Lecture Note in Physics; Springer: Berlin/Heidelberg, Germany, 1980, Volume 320, pp. 57–65.
33. Scheibe, T.; Yabusaki, S. Scaling of flow and transport behavior in heterogeneous groundwater systems. *Adv. Water Resour.* **1998**, *22*, 223–238. [CrossRef]
34. Durlofsky, L.; Efendiev, Y.; Ginting, V. An adaptive local–global multiscale finite volume element method for two-phase flow simulations. *Adv. Water Resour.* **2007**, *30*, 576–588. [CrossRef]
35. Chen, Y.; Mallison, B.T.; Durlofsky, L.J. Nonlinear two-point flux approximation for modeling full-tensor effects in subsurface flow simulations. *Comput. Geosci.* **2008**, *12*, 317–335. [CrossRef]
36. Vasilyeva, M.; Leung, W.T.; Chung, E.T.; Efendiev, Y.; Wheeler, M. Learning macroscopic parameters in nonlinear multiscale simulations using nonlocal multicontinua upscaling techniques. *J. Comput. Phys.* **2020**, *412*, 109323. [CrossRef]
37. Jenny, P.; Lee, S.H.; Tchelepi, H.A. Adaptive multiscale finite-volume method for multiphase flow and transport in porous media. *Multiscale Model. Simul.* **2005**, *3*, 50–64. [CrossRef]
38. Hajibeygi, H.; Bonfigli, G.; Hesse, M.A.; Jenny, P. Iterative multiscale finite-volume method. *J. Comput. Phys.* **2008**, *227*, 8604–8621. [CrossRef]

39. Hughes, T.J.; Feijóo, G.R.; Mazzei, L.; Quincy, J.B. The variational multiscale method?a paradigm for computational mechanics. *Comput. Methods Appl. Mech. Eng.* **1998**, *166*, 3–24. [CrossRef]
40. Abdulle, A.; Weinan, E.; Engquist, B.; Vanden-Eijnden, E. The heterogeneous multiscale method. *Acta Numer.* **2012**, *21*, 1–87. [CrossRef]
41. Chung, E.T.; Efendiev, Y.; Li, G.; Vasilyeva, M. Generalized multiscale finite element methods for problems in perforated heterogeneous domains. *Appl. Anal.* **2016**, *95*, 2254–2279. [CrossRef]
42. Chung, E.T.; Leung, W.T.; Vasilyeva, M.; Wang, Y. Multiscale model reduction for transport and flow problems in perforated domains. *J. Comput. Appl. Math.* **2018**, *330*, 519–535. [CrossRef]
43. Chung, E.T.; Efendiev, Y.; Vasilyeva, M.; Wang, Y. A multiscale discontinuous Galerkin method in perforated domains. *Proc. Inst. Math. Mech.* **2016**, *42*, 212–229.
44. Chung, E.T.; Vasilyeva, M.; Wang, Y. A conservative local multiscale model reduction technique for Stokes flows in heterogeneous perforated domains. *J. Comput. Appl. Math.* **2017**, *321*, 389–405. [CrossRef]
45. Vasilyeva, M.; Alekseev, V.; Chung, E.T.; Efendiev, Y. Multiscale dimension reduction for flow and transport problems in thin domain with reactive boundaries. *J. Comput. Phys.* **2021**, *442*, 110512. [CrossRef]
46. Spiridonov, D.; Vasilyeva, M.; Wang, M.; Chung, E.T. Mixed Generalized Multiscale Finite Element Method for flow problem in thin domains. *J. Comput. Appl. Math.* **2022**, *416*, 114577. [CrossRef]
47. Mehmani, Y.; Tchelepi, H.A. Multiscale computation of pore-scale fluid dynamics: Single-phase flow. *J. Comput. Phys.* **2018**, *375*, 1469–1487. [CrossRef]
48. Mehmani, Y.; Tchelepi, H.A. Multiscale formulation of two-phase flow at the pore scale. *J. Comput. Phys.* **2019**, *389*, 164–188. [CrossRef]
49. Wu, X.; Efendiev, Y.; Hou, T.Y. Analysis of upscaling absolute permeability. *Discret. Contin. Dyn. Syst. B* **2002**, *2*, 185–204. . [CrossRef]
50. Logg, A.; Mardal, K.A.; Wells, G. *Automated Solution of Differential Equations by the Finite Element Method: The FEniCS Book*; Springer Science & Business Media: Berlin/Heidelberg, Germany, 2012; Volume 84.
51. Geuzaine, C.; Remacle, J.F. Gmsh: A 3-D finite element mesh generator with built-in pre-and post-processing facilities. *Int. J. Numer. Methods Eng.* **2009**, *79*, 1309–1331. [CrossRef]
52. Ayachit, U. *The Paraview Guide: A Parallel Visualization Application*; Kitware, Inc.: Clifton Park, NY, USA, 2015.
53. Lei, D.; Sun, H.; Zhang, Y.; Blaszczyk, T.; Yu, Z. Upscaling Solute Transport in Rough Single-Fractured Media with Matrix Diffusion Using a Time Fractional Advection-Dispersion Equation. *J. Hydrol.* **2023**, *627*, 130280. [CrossRef]
54. Liu, F.; Anh, V.; Turner, I. Numerical solution of the space fractional Fokker–Planck equation. *J. Comput. Appl. Math.* **2004**, *166*, 209–219. [CrossRef]
55. Zhao, Z.; Zheng, Y. Numerical Approximation for Fractional Neutron Transport Equation. *J. Math.* **2021**, *2021*, 6676640. [CrossRef]
56. Alaoui, M.K.; Nonlaopon, K.; Zidan, A.; Khan, A.; Shah, R. Analytical investigation of fractional-order Cahn-Hilliard and Gardner equations using two novel techniques. *Mathematics* **2022**, *10*, 1643. [CrossRef]
57. Sunthrayuth, P.; Zidan, A.M.; Yao, S.W.; Shah, R.; Inc, M. The comparative study for solving fractional-order Fornberg–Whitham equation via $\rho$-Laplace transform. *Symmetry* **2021**, *13*, 784. [CrossRef]
58. Zidan, A.M.; Khan, A.; Shah, R.; Alaoui, M.K.; Weera, W. Evaluation of time-fractional Fisher's equations with the help of analytical methods. *Aims Math.* **2022**, *7*, 18746–18766. [CrossRef]
59. Deng, H.; Molins, S.; Trebotich, D.; Steefel, C.; DePaolo, D. Pore-scale numerical investigation of the impacts of surface roughness: Upscaling of reaction rates in rough fractures. *Geochim. Cosmochim. Acta* **2018**, *239*, 374–389. [CrossRef]


**Disclaimer/Publisher's Note:** The statements, opinions and data contained in all publications are solely those of the individual author(s) and contributor(s) and not of MDPI and/or the editor(s). MDPI and/or the editor(s) disclaim responsibility for any injury to people or property resulting from any ideas, methods, instructions or products referred to in the content.